



# Absorber Design and Optimization of Kinetic Inductance Detectors for the Terahertz Intensity Mapper

R. Nie<sup>1</sup> · R. M. J. Janssen<sup>2,3</sup> · C. M. Bradford<sup>2,3</sup> · J. P. Filippini<sup>1</sup> · S. Hailey-Dunsheath<sup>3</sup> · C. M. McKenney<sup>4</sup> · J. E. Aguirre<sup>5</sup> · J. S. Bracks<sup>5</sup> · A. J. Corso<sup>5</sup> · J. Fu<sup>1</sup> · C. Groppi<sup>6</sup> · J. Hoh<sup>6</sup> · R. P. Keenan<sup>7</sup> · L.-J. Liu<sup>3</sup> · I. N. Lowe<sup>7</sup> · D. P. Marrone<sup>7</sup> · P. Mauskopf<sup>6</sup> · J. Redford<sup>3</sup> · I. Trumper<sup>8</sup> · J. D. Vieira<sup>1</sup>

Received: 1 November 2021 / Accepted: 13 May 2022 / Published online: 15 June 2022

© The Author(s), under exclusive licence to Springer Science+Business Media, LLC, part of Springer Nature 2022

## Abstract

We discuss the design and optimization of the absorber for Terahertz Intensity Mapper, a balloon-borne kinetic inductance detector spectrometer. The novel “chain-link” absorber design offers excellent performance, independent optimization for both polarizations, and robust fabrication. Electromagnetic simulations indicate in-band absorption efficiency over  $\sim 90\%$  in both linear polarization modes. DC measurements on different film thicknesses indicate the desired sheet resistance.

**Keywords** Electromagnetic simulations · Kinetic inductance detector · Terahertz Intensity Mapper

---

✉ R. Nie  
rongnie2@illinois.edu

<sup>1</sup> University of Illinois at Urbana-Champaign, Urbana, IL 61801, USA

<sup>2</sup> Jet Propulsion Laboratory, California Institute of Technology, Pasadena, CA 91109, USA

<sup>3</sup> California Institute of Technology, Pasadena, CA 91125, USA

<sup>4</sup> University of Colorado, Boulder, CO 80303, USA

<sup>5</sup> University of Pennsylvania, Philadelphia, PA 19104, USA

<sup>6</sup> Arizona State University, Tempe, AZ 85287, USA

<sup>7</sup> University of Arizona, Tucson, AZ 85721, USA

<sup>8</sup> Intuitive Optical Design Lab LLC, Tucson, AZ 85701, USA

## 1 Introduction

Understanding the history of star formation throughout cosmic time would provide significant insights into the processes of galactic evolution. The far-infrared (FIR) wavelength band contains valuable information to address this question because (A) FIR spectral lines are relatively un-extincted, and (B) half of the total energy output from the cosmic star formation has been absorbed by interstellar dust and re-emitted in the FIR [1, 2].

The **Terahertz Intensity Mapper (TIM)** is a NASA FIR balloon mission, which serves as a vital technological and scientific stepping stone to future orbital missions such as the Origins Space Telescope [3]. TIM aims to constrain the cosmic star formation history by measuring redshifted [CII] and other diagnostic FIR lines at cosmic noon ( $0.5 < z < 1.5$ ) [4]. To achieve this, TIM carries a 240–420  $\mu\text{m}$   $R \sim 250$  grating spectrometer fed by a 2 m warm reflector, partitioned into a long wavelength (LW: 317–420  $\mu\text{m}$ ) and a short wavelength (SW: 240–317  $\mu\text{m}$ ) module.

To approach photon-noise-limited performance with high scalability, TIM employs feedhorn coupled aluminum kinetic inductance detector (KID) arrays operated at 250 mK. KIDs are non-equilibrium superconducting detectors consisting of thin-film, high-Q micro-resonators that absorb incident radiation and respond by changing resonance frequency and quality factor [5]. Due to high resonance quality factors, their primary advantage is built-in frequency division multiplexing, allowing large numbers of KIDs to be read out on a single RF/microwave circuit.

In this paper, we will present a novel absorber design (Sect. 2), which we call the “chain-link” (CL) design and discuss its advantages over the previous “quasi-mesh” (QM) design. We optimize the CL design using electromagnetic simulations and present the performance for both SW and LW in Sect. 3. A key parameter for the CL performance is the aluminum resistance, and the material’s DC measurements are in Sect. 4. We will summarize and give an outlook in Sect. 5. Throughout this work, we follow the figure format and, in some cases, even the wording of our previous publication [6].

## 2 Absorber Design

Our KIDs design uses a separate inductor and capacitor to form a resonator, often referred to as lumped element KID [7]. Following our previous QM design for LW module [6, 8, 9], the inductor is a 500 nm wide aluminum meander patterned onto a silicon wafer with integrated back-short (Fig. 1). The inductor is front-side illuminated by a conical feedhorn, which essentially also works as an absorber for photon absorption. The absorber is identical for each pixel on the same module, and the capacitors are different for each pixel and are designed to achieve 500–2000 MHz readout frequencies.

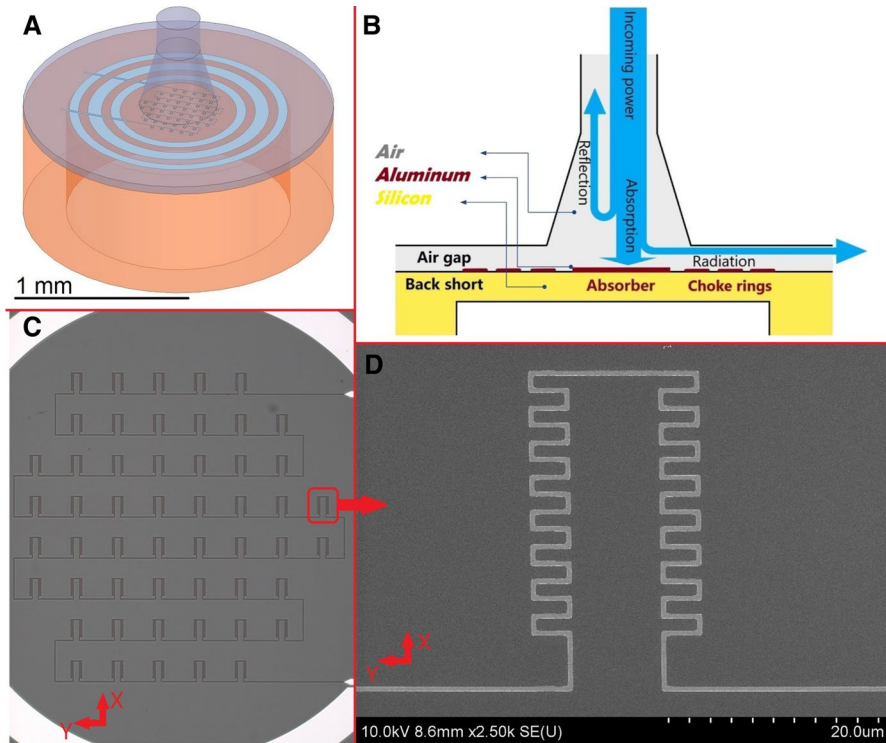


**Fig. 1** **A** 3-D rendering of a single absorber pixel in HFSS. The circular rings around the absorber are the choke structure to reduce the cross-talk between pixels. **B** Side view cartoon of a single pixel from LW band. Photons propagate from the top port through a flared circular waveguide onto the aluminum meander, which is front-side illuminated. A back-short layer of 100 nm aluminum is sputtered on the other side of the silicon wafer. **C** Top view of the fabricated meander geometry under an optical microscope. One meander consists of 52 identical unit cells. Also shown in part in this image is the circumference of the inner choke ring. **D** Zoomed in image of a single unit cell under a scanning electron microscope. SW band shares similar geometry, but the relevant scale is reduced by 1.323 (circular waveguide radius, absorber size, choke ring radius, etc.). The exceptions are air gap and line width remaining 50 and 0.5  $\mu\text{m}$ , respectively. The back-short thickness for LW and SW is 27 and 20  $\mu\text{m}$ , respectively. (Color figure online.)

Instead of the QM design, we have developed an improved absorber we call the CL design, which utilizes reactive aspects of the meandered structure to boost the absorption efficiency. The horizontal ( $y$  axis in Fig. 1C, D) parallel baselines provide photon absorption along the horizontal direction but result in almost no efficiency for the vertical ( $x$  axis) polarization [6]. We first add inverted 'U' shape bumps to the straight line to provide efficiency in both linear polarizations. However, the impedance in the

vertical direction is still insufficient. We then add smaller winglet structures on the 'U' bump to create a longer current path. One of the immediate advantages compared to the previous QM design is there are relatively more parameters to tune, and it enables more independent optimization over  $x$  and  $y$ -polarizations. The next section presents the detailed considerations of the optimization over these parameters.

### 3 Finite-Element Simulations

#### 3.1 Optimization Considerations

We carried out a program of simulations using the commercial finite-element method electromagnetic software ANSYS-HFSS.<sup>1</sup> To efficiently achieve the best design, we perform the optimization in the following steps of increasing the size scale: (i) To maximize the in-band absorption efficiency in both polarizations, we investigate the parameters for the unit cell (Fig. 1D). We optimized over six parameters for the design of a unit cell: line width, cell pitch distance, line distance between two 'U' bump arms, length of the 'U' bump arms, length of the winglets, and the neck distance between the straight line and the first winglet, with emphasis on the last four parameters since this is the novel part of the CL design. The line width and cell pitch distance are first set to be  $0.5\ \mu\text{m}$  and  $60\ \mu\text{m}$ , respectively, mainly based on the initial design [6]. Then, we sweep the four-dimensional parameter space with the last four items. The optimized values are  $9.0\ \mu\text{m}$ ,  $30.0\ \mu\text{m}$ ,  $4.0\ \mu\text{m}$ , and  $5.3\ \mu\text{m}$ , respectively. Note that there are other parameters to change, for example, the number of winglets. As we proceed with these aforementioned six parameters and the result reaches our initial design goal, we did not implement optimization over more parameters. (ii) The target inductor volume for these KIDs is  $100\ \mu\text{m}^3$ , which is sufficient to achieve a detector noise equivalent power  $< 10^{-17}\ \text{W Hz}^{-1/2}$  as shown by simulations and previous experimental results [9, 11]. To reduce the detector volume and fit into the circular choke rings, we simulate different total numbers of identical cells and the overall shape of the absorber. We start the absorber design in a square shape with  $8 \times 8$  unit cells, and then, we remove 12 cells from the corners and result in a 52-cell design. (iii) To minimize the cross-talk between pixels, we study the parameters such as the width of each choke ring and the thickness of the air gap. (iv) We finally simulate the entire pixel together and "fine-tune" some of the parameters to ensure the performance is still within our proposed target.

#### 3.2 Simulation Results

Figure 2 shows the performance of the present design. The incoming power from the waveguide is distributed to five different parts, each measured independently in HFSS: energy dissipated on the absorber ( $P_{ab}$ ), reflection back to the waveguide

<sup>1</sup> <https://www.ansys.com/products/electronics/ansys-hfss>, version 19.2.

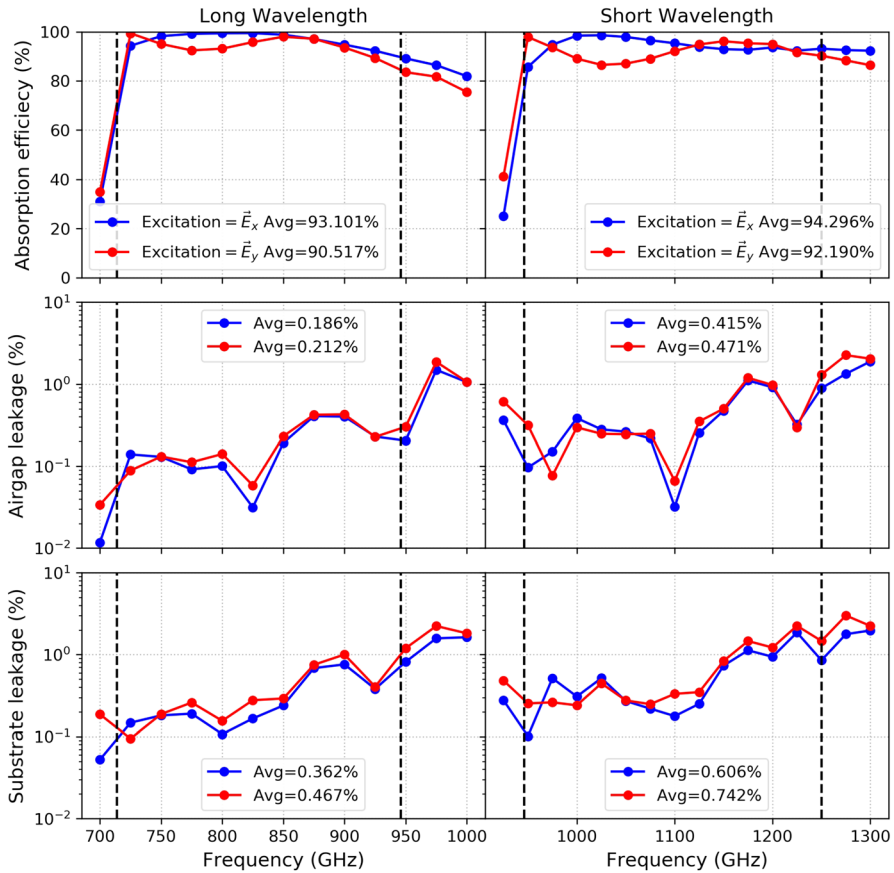


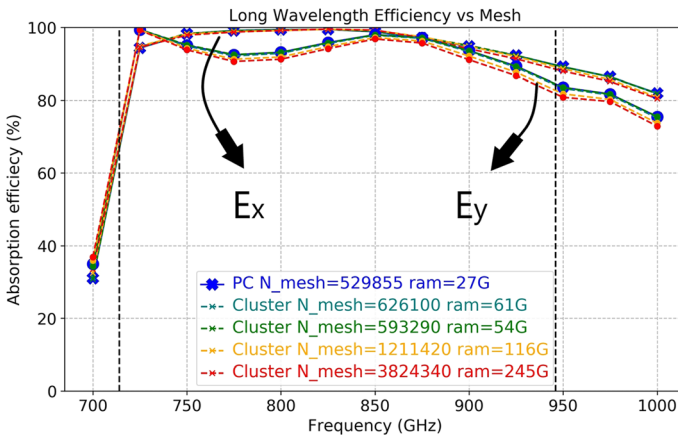
**Fig. 2** Simulation results of the optimized design for the LW and SW models. The waveguide is excited by a single circular  $TE_{11}$  mode, and both x and y excitations are plotted. *Left and right* columns are LW and SW module, respectively. *Top, middle, and bottom* rows are absorption efficiency, leakage through air gap, and leakage through silicon wafer, respectively. All powers are normalized to the input power. Vertical lines delimit the desired bandwidth. (Color figure online.)

( $|S_{11}|^2$ ), absorption by the choke rings ( $P_{cr}$ ), and radiation escaping the pixel through the air gap ( $P_{ag}$ ) and the substrate ( $P_{sb}$ ). The absorbed and radiated powers are defined as  $P_i = \int Re(\mathbf{S} \cdot \mathbf{n})dA_i$ , where  $\mathbf{S}$  is the Poynting vector, and  $\mathbf{n}$  is the unit outward normal vector of each surface  $A_i$ . The average optical efficiency over both LW and SW modules is above 90%. For each module, absorption at low frequencies is suppressed by the waveguide cut-off frequency. Leakage through the air gap and substrate indicates sub-percent cross-talk. The higher leakage at higher frequencies might be caused by the shorter wavelength compared to the constant physical dimensions of air gap and substrate thickness.

In addition to the excellent performance, CL design also benefits from other aspects than the QM design: (i) QM design has relatively few parameters to tune

**Table 1** Performance comparison for the previous and new designs

Module	Design	Minimum line spacing ( $\mu\text{m}$ )	Air gap ( $\mu\text{m}$ )	Line width ( $\mu\text{m}$ )	$R_s$ ( $\Omega/\square$ )	Efficiency (%)
Long Wavelength	Quasi-Mesh	0.3	25	0.4	2	> 80
Long Wavelength	Chain-Link	1.2	50	0.5	1	> 90
Short Wavelength	Chain-Link	0.7	50	0.5	1	> 90

**Fig. 3** LW simulation on computing cluster with finer mesh. *Blue line* labeled as PC has the same mesh density as Fig. 2. (Color figure online.)

and non-trivial dependence of polarization. In contrast, the winglet structure in CL design provides more parameters to tune and is relatively independent to orthogonal polarizations. (ii) To provide a single current path, required to function as a KID's inductor and still remain capacitively connected for the absorption, QM design relies on tight gap between mesh vertices. The CL design improves this constraint by a factor of 4. (iii) The air gap is  $2\times$  larger, which reduces the possibility of unwanted shorts between detector array and feed-horn block and improves the machine tolerance for detector packaging. See Liu et al. [10] for details. (iv) Line width for CL design is  $100\text{ nm}$  wider ( $500\text{ nm}$  vs.  $400\text{ nm}$ ) than QM design. The line width is unchanged for the SW module and still results in high efficiency. (v) The assumed sheet resistance is lower for the CL design, which is desired because achieving low sheet resistance is easier than high resistance for the proposed material of aluminum. This was also the initial challenge when inherited from the MAKO titanium nitride ( $R_{sTiN}/R_{sAl} \sim 100$ ) design. We note here that our first fabrication of the aluminum absorber resulted in narrower line width  $\sim 0.4\mu\text{m}$ , and lower sheet resistance  $R_s \sim 1\Omega/\square$ . We thus perform additional simulations under the variations of the line width, sheet

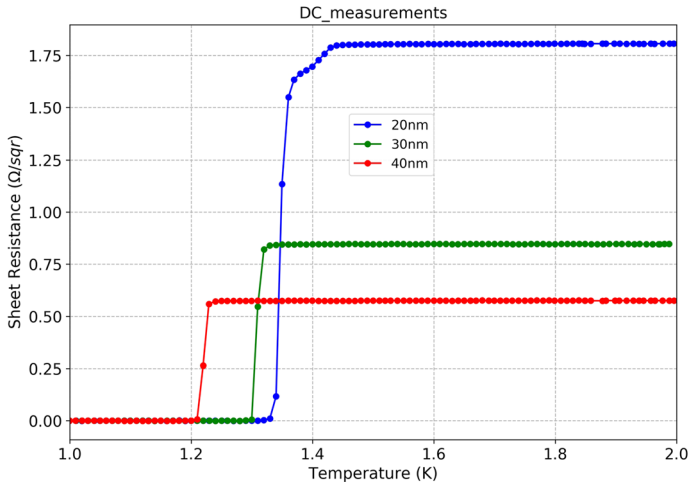


**Fig. 4** Aluminum sheet resistance as a function of temperature for three different film thicknesses. (Color figure online.)

resistance, and air gap thickness. The results show that the CL performance is stable. Table 1 summarizes the improvements compared to the previous design. The QM design results in even lower efficiency with  $R_s = 1\Omega/\square$

### 3.3 Convergence Study

FEM simulation results may be sensitive to the number or size of the meshed elements, especially in a model with a fine structure. We thus repeat the simulation at higher mesh densities with a computing cluster. Figure 3 *left* shows that the cluster computation provides  $7\times$  finer mesh and suggests that the coarser (but adaptive) mesh used in Fig. 2 captures the absorber's behavior with good fidelity.

## 4 DC Measurements

To measure the performance of detectors with different film thicknesses, we have fabricated LW testing detector array with 20-, 30-, and 40- nm-thick aluminum in the JPL Microdevices Laboratory. This section presents the DC measurement results of the transition temperature  $T_c$  and sheet resistance  $R_s$ , which are essential parameters to model resonators following the standard application of Mattis-Bardeen theory and test the assumption used in optical efficiency simulation. We have also fabricated and

cryogenically tested a 45-pixel prototype array. The detailed dark and optical testing results are presented in Janssen et al. [11].

The superconductivity measurements were performed in Quantum Design Physical Property Measurement System (PPMS). A helium-3 insert extends the accessible temperature to 1 K. Multiple standard four-point measurements of a variety of DC test structures on the 30 nm samples deposited along with the same detector array show a  $T_c = 1.28 \pm 0.04$  K and  $R_s = 0.7\Omega/\square$ . We then focused on the 1000  $\mu\text{m}$  long, 2  $\mu\text{m}$  wide DC testing structure and measured aluminum samples with different film thicknesses, as Fig. 4 shows. Each measurement was performed at a stable temperature with a  $-0.01$  K temperature increment and 2  $\mu\text{A}$  excitation current. The  $T_c$  of these films increased with decreasing film thickness. The change of  $R_s$  indicates that we can approach the desired  $R_s = 1\Omega/\square$  sheet resistance by adjusting film thickness. The result is similar to Chubov et al. [12].

## 5 Summary

This study has demonstrated a meandered aluminum KID absorber forming CL design for TIM with high absorption efficiency ( $> 90\%$ ) in both  $x$  and  $y$ -polarizations. The power loss through the wafer and air gap is low, indicating minimal optical cross-talk between pixels. Compared to the previous QM design, CL design improves robustness and optical efficiency. The first prototype has been fabricated and cryogenically tested. DC measurements on different film thicknesses indicate the expected transition temperature and desired sheet resistance. We are currently optically testing the LW module. This effort will be the subject of a future publication.

**Acknowledgements** TIM is supported by NASA under grant 80NSSC19K1242, issued through the Science Mission Directorate. R.M.J. Janssen is supported by an appointment to the NASA Postdoctoral Program at the NASA Jet Propulsion Laboratory, administered by Universities Space Research Association under contract with NASA. The material presented in this work was carried out in part in the Micro-Nano-Mechanical Systems Cleanroom Laboratory within the Department of Mechanical Science and Engineering at the University of Illinois. The SEM imaging and  $T_c$  measurements were carried out in part in the Materials Research Laboratory Central Research Facilities, University of Illinois. Part of this research was carried out at the Jet Propulsion Laboratory, California Institute of Technology, under a contract with the National Aeronautics and Space Administration (80NM0018D0004).

## References

1. M.G. Hauser, E. Dwek, *Annu. Rev. Astron. Astrophys.* **39**, 249 (2001). <https://doi.org/10.1146/annurev.astro.39.1.249>
2. G. Lagache, J.L. Puget, H. Dole, *Annu. Rev. Astron. Astrophys.* **43**, 727 (2005). <https://doi.org/10.1146/annurev.astro.43.072103.150606>
3. M. Meixner, A. Cooray, D. Leisawitz, J. Staguhn, L. Armus, C. Battersby, J. Bauer, E. Bergin, C.M. Bradford, K. Ennico-Smith, J. Fortney, T. Kataria, G. Melnick, S. Milam, D. Narayanan, D. Padgett, K. Pontoppidan, A. Pope, T. Roellig, K. Sandstrom, K. Stevenson, K. Su, J. Vieira, E. Wright, J. Zmuidzinas, K. Sheth, D. Benford, E.E. Mamajek, S. Neff, E. De Beck, M. Gerin,



- F. Helmich, I. Sakon, D. Scott, R. Vavrek, M. Wiedner, S. Carey, D. Burgarella, S.H. Moseley, E. Amatucci, R.C. Carter, M. DiPirro, C. Wu, B. Beaman, P. Beltran, J. Bolognese, D. Bradley, J. Corsetti, T. D'Asto, K. Denis, C. Derkacz, C.P. Earle, L.G. Fantano, D. Folta, B. Gavares, J. Generie, L. Hilliard, J.M. Howard, A. Jamil, T. Jamison, C. Lynch, G. Martins, S. Petro, D. Ramsbacher, A. Rao, C. Sandin, E. Stoneking, S. Tompkins, and C. Webster, (2019) [arXiv:1912.06213v2](https://arxiv.org/abs/1912.06213v2)
4. J. Vieira, J. Aguirre, C. M. Bradford, J. Filippini, C. Groppi, D. Marrone, M. Bethermin, T.C. Chang, M. Devlin, O. Dore, J. Fu, S. Hailey-Dunsheath, G. Holder, G. Keating, R. Keenan, E. Kovetz, G. Lagache, P. Mauskopf, D. Narayanan, G. Popping, E. Shirokoff, R. Somerville, I. Trumper, B. Uzgil, and J. Zmuidzinas, *ISSTT2019*, (2019)
  5. P.K. Day, H.G. LeDuc, B.A. Mazin, A. Vayonakis, J. Zmuidzinas, *Nature* **425**, 817 (2003). <https://doi.org/10.1038/nature02037>
  6. R. Nie, R.M.J. Janssen, C.M. Bradford, J.P. Filippini, S. Hailey-Dunsheath, *IEEE Trans. Terahertz Sci. Technol.* **10**(6), 712 (2020). <https://doi.org/10.1109/TTHZ.2020.3022020>
  7. S. Doyle, P. Mauskopf, J. Naylon, A. Porch, C. Duncombe, *J. Low Temp. Phys.* **151**, 530 (2008). <https://doi.org/10.1007/s10909-007-9685-2>
  8. C.M. McKenney, H.G. Leduc, L.J. Swenson, P.K. Day, B.H. Eom, J. Zmuidzinas, *Proc. SPIE* **8452**, 84520S (2012). <https://doi.org/10.1117/12///.925759>
  9. S. Hailey-Dunsheath, A.C.M. Barlis, J.E. Aguirre, C.M. Bradford, J.G. Redford, T.S. Billings, H.G. LeDuc, C.M. McKenney, M.I. Hollister, *J. Low Temp. Phys.* **193**, 968 (2018). <https://doi.org/10.1007/s10909-018-1927-y>
  10. L.-J. Liu, R.M.J. Janssen, J. Fu, J.E. Aguirre, J.S. Bracks, C.M. Bradford, A.J. Corso, J.P. Filippini, C. Groppi, S. Hailey-Dunsheath, J. Hoh, R.P. Keenan, I.N. Lowe, D.P. Marrone, P. Mauskopf, R. Nie, J. Redford, I. Trumper, and J.D. Vieira, *J. Low Temp. Phys. (This Special Issue)* (2021)
  11. R.M.J. Janssen, R. Nie, B. Bumble, L.-J. Liu, J. Redford, J.P. Filippini, C.M. Bradford, S. Hailey-Dunsheath, J.E. Aguirre, J.S. Bracks, A.J. Corso, J. Fu, C. Groppi, J. Hoh, R.P. Keenan, I.N. Lowe, D.P. Marrone, I. Trumper, and J.D. Vieira, *J. Low Temp. Phys. (This Special Issue)* (2021)
  12. P.N. Chubov, V.V. Eremenko, Yu.A. Pilipenko, *Sov. Phys. J. Exp. Theor. Phys* **28**, 389 (1969)

**Publisher's Note** Springer Nature remains neutral with regard to jurisdictional claims in published maps and institutional affiliations.